energies

Article

Performance Analysis of Synchronous Reluctance Motor with Limited Amount of Permanent Magnet

Duc-Kien Ngo [1] and Min-Fu Hsieh [2,*]

[1] Department of Systems and Naval Mechatronic Engineering, National Cheng Kung University, Tainan 70101, Taiwan; eng.duckien.ngo@gmail.com
[2] Department of Electrical Engineering, National Cheng Kung University, Tainan 70101, Taiwan
* Correspondence: mfhsieh@mail.ncku.edu.tw; Tel.: +866-06-275-7575 (ext. 62366)

Received: 11 August 2019; Accepted: 9 September 2019; Published: 11 September 2019

Abstract: This paper analyzes the performance of a synchronous reluctance motor (SynRM) equipped with a limited amount of a permanent magnet (PM). This is conventionally implemented by inserting PMs in rotor flux barriers, and this is often called the PM-assisted SynRM (PMa-SynRM). However, common PMa-SynRMs could be vulnerable to irreversible demagnetization. Therefore, motor performance and PM demagnetization should be simultaneously considered, and this would require the PM to be properly arranged. In this paper, various rotor configurations are carefully studied and compared in order to maximize the motor performance, avoid irreversible demagnetization and achieve higher PM utilization. Moreover, the field weakening capability is investigated and improved by regulating armature excitation. A particular rotor type with flux intensification was found to possess higher PM utilization, lower demagnetization possibility with fairly high performance. Thus, suitable rotor configurations are recommended for certain applications.

Keywords: SynRM; irreversible demagnetization; PMa-SynRM; flux intensifying

1. Introduction

The synchronous reluctance motor (SynRM), with its robustness, high overload capability and low cost, has become a popular research target for many years [1–4]. However, the relatively lower torque/power density and power factor are the inherent disadvantages of SynRMs [5–7] compared to a permanent magnet synchronous machine (PMSM). To overcome such weaknesses, a permanent magnet (PM) can be inserted into the rotor of the SynRMs with a modest volume, which leads to the birth of a type of motor called the permanent magnet assisted synchronous reluctance motor (PMa-SynRM) [8–11]. With the increasing number of related research works, the PMa-SynRM has become a popular choice in some applications and can be an alternative to a SynRM or PMSM [12–15].

Generally, the PMs inserted inside the rotor flux barriers produce a negative flux linkage along the q-axis. The q-axis inductance L_q is usually low due to the multiple flux barriers. The permanent magnet (PM) flux linkage (the flux linkage due to PM solely) promotes the rotation of the flux linkage vector, and therefore the voltage vector goes close to the current vector to increase the power factor [9]. The PM flux linkage also contributes to torque production so that the total torque increases. However, the volume/size of the added PM needs to be limited to avoid the motor becoming an interior permanent magnet synchronous motor (IPMSM) [16], which could also increase the cost. Nevertheless, the volume/size of the PM should not be too small to achieve the desired torque and power density, or to be vulnerable to irreversible demagnetization [10].

For SynRMs or PMa-SynRMs, various design possibilities can be considered, e.g., the number of flux barriers, with or without PMs, rare earth or other types of PM materials or the amount of PM employed. In an effort to standardize the design process of SynRMs and PMa-SynRMs, Bianchi et al. [11] proposed a series of steps that are synthesized from some example studies [11,17–20], where the inward PMs (near the rotor shaft) are larger than the outward ones to improve flux flows and avoid demagnetization. This PM arrangement is considered as a common trend for the PMa-SynRM rotor design.

Some motor designs presented in previous research [10,11,21–23] using either rare-earth or ferrite PMs are summarized in Table 1, including their ratio of PM-to-motor volume and torque density. It can be observed that the variety of rotor designs and PM arrangements is rich in these motors. However, the first four motors listed in Table 1 [10,11,21,22] employ a relatively large PM volume compared to the motor studied in Reference [23]. Furthermore, the PM size in the motor in Reference [23] is purposefully made identical for all the PM layers to reduce the manufacturing cost, which is different from common designs. The multiple flux barrier design allows the torque density of this motor to reach 28.1 Nm/L with PM taking only 0.95% of the motor volume by assuming sufficient cooling is applied, as shown in Table 1. However, as mentioned in Reference [16], the low PM volume and high excitation current could lead to its negligible contribution in torque production due to the low PM-torque-to-total-torque ratio and high probability of irreversible demagnetization with field-weakening applied. In addition, since the armature current I_s is far from the characteristic current I_{ch} on d-axis [24], the constant power speed range (CPSR) could become relatively low for PMa-SynRM with a little amount of PM. From the above discussions, it is necessary to propose a solution to improve the performance of this type of motor in terms of PM utilization, demagnetization resistivity and field weakening capability.

Table 1. The reference motor parameters and torque production.

Reference Motor Source	**[10]**	**[11]**	**[21]**	**[22]**	**[23]**
Stator diameter (mm)	150	200	125	112	160
Stack length (mm)	105	40	27	40	120
Motor volume (L)	1.856	1.257	0.331	0.394	2.413
PM volume (L)	0.066	0.077	0.013	0.009	0.023
PM-to-Motor volume ratio (%)	3.58	6.13	3.93	2.28	0.95
PM material type	Rare earth	Ferrite	Ferrite	Rare earth	Rare earth
Number of poles	4	4	4	4	4
Number of flux barriers for each pole	4	3	2	1	5
Number of PM layers	4	3	2	1	4
PM size between layers	Unequal	Unequal	Unequal	-	Equal
Torque (Nm)	17.9	12.47	1.27	4.54	67.8
Torque density (Nm/L)	9.7	9.9	3.8	11.5	28.1

Therefore, in this paper, several motor models based on a prototyped PMa-SynRM [23] with various PM arrangements using limited amount of PM are analyzed in detail. The analysis concentrates on the effect of the PM position on the magnetic distribution, inductances, torque production, torque/power-speed curves and magnetization characteristics. The armature current is also adjusted for observation on the correlation between the electrical and magnetic parameters affecting the motor performance. From the above analysis, this paper aims to achieve a high PM utilization rate to produce torque though a limited amount of PMs in a more efficient way. Demagnetization can also be avoided under high performance operations. The analysis was conducted using finite element analysis (FEA), which has been partially validated using previous experimental studies [23]. Note that differing from Reference [23], where the evaluation was only conducted for a fixed rotor structure, this paper makes a complete analysis with a sufficient number of models in order to make proper suggestions for the improvement of SynRM performance. In Reference [25], the PM volume was optimized for predetermined field-intensified PM machines. Here, in the present study, the models investigated cover not only conventional PMa-SynRMs, but also the novel flux-intensifying PMa-SynRMs [26]. In what follows, the terms flux-intensification, flux-intensifying and flied-intensified are all abbreviated as FI. In addition, by investigating over an existing prototype, the analysis can be better convincing. The comparisons can also be made to highlight the novelty of the current analysis.

This paper is organized as follows. The mathematical model and the configuration of the motor models are presented first in Section 2. Then, the investigation for the influence of PM positions on motor characteristics is carried out in Section 3, followed by the comparison of some motor models in Section 4. Section 5 presents the discussions over these investigated models. Finally, the paper is concluded by making suggestions for the design of such motors in Section 6.

2. Mathematical Model and Configuration of Investigated Motors

2.1. Mathematical Modeling of Investigated Motors

A conventional SynRM with a limited amount of PM embedded along the flux barriers, i.e., facing the physical q-axis, is called the first PM arrangement (hereafter denoted Type 1), as shown in Figure 1a. In contrast, when PM is added crossing the flux barriers, i.e., facing the d-axis, it is called the second PM arrangement (hereafter denoted Type 2), as the example illustrated in Figure 1b. For the Type 1 rotor, the flux linkage produced by the PM is arranged against the q-axis armature flux linkage, while for the Type 2 rotor, the PM flux linkage complements the d-axis armature flux linkage. The Type 2 motor can thus be called the flux-intensifying PMa-SynRM (FI-PMa-SynRM) [26].

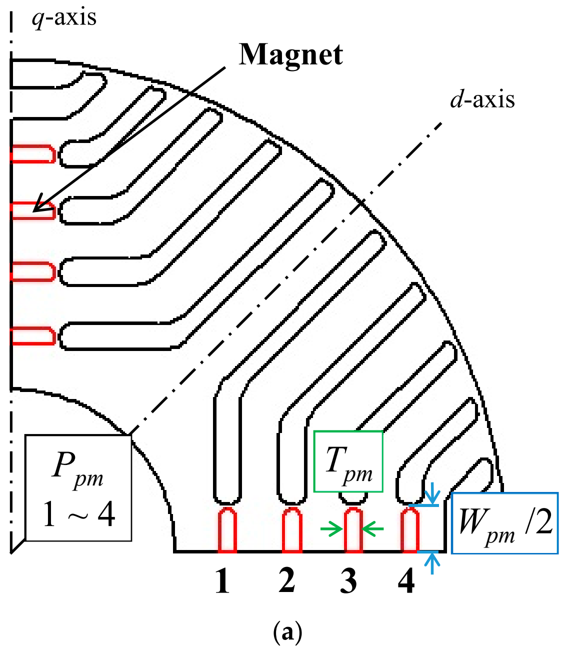

Figure 1. Rotor configurations: (**a**) The first permanent magnet (PM) arrangement (Type 1); (**b**) The second PM arrangement (Type 2).

Assuming that the iron saturation and the cross-coupling effect are neglected, the stator dynamic voltage equations for synchronous machines in the d-q frame [27,28] can be expressed as:

$$v_d = R_s i_d + \frac{d\lambda_d}{dt} - \omega\lambda_q \quad (1)$$

$$v_q = R_s i_q + \frac{d\lambda_q}{dt} + \omega\lambda_d \quad (2)$$

where the subscripts d and q represent the d- and q-axis, respectively, i_d and i_q are the currents, λ_d and λ_d are the flux linkages, R_s is the phase resistance, and ω is the electrical angular speed.

Equations (1) and (2) are general voltage equations for synchronous machines. To be applied to the two types of motors mentioned above, the flux linkages λ_d and λ_q in (1) and (2) need to be further discussed since the PMs are arranged differently in these two types of motors. For the Type 1 motors, as previously mentioned, the PMs are arranged in q-axis against the stator flux due to the q-axis current (i_d), and therefore the flux linkages in the d-q frame can be expressed as:

$$\lambda_d = L_d i_d, \lambda_q = L_q i_q - \lambda_m \tag{3}$$

where L_d and L_q are the stator inductances in the d-q frame, and λ_m is the PM flux linkage. Note that L_d and L_q do not take into account the PM flux linkage but only the flux linkage produced by i_d and i_q. For the Type 2 motors, the PMs are placed in the d-axis to complement the stator flux and thus the flux linkages are given as:

$$\lambda_d = L_d i_d + \lambda_m, \lambda_q = L_q i_q \tag{4}$$

From (3) and (4), the flux-weakening nature for the Type 1 motors and the flux-intensifying characteristics for the Type 2 can be clearly observed.

Figure 2 presents the equivalent circuits for the Type 1 [27] and Type 2 motors. As can be seen, the two types of motors have a difference in PM flux linkages. The phasor diagrams for Type 1 [9] and Type 2 are illustrated in Figure 3a,b, respectively, with the winding resistance being neglected [9,29]. Therefore, the voltage equations can be further expressed as:

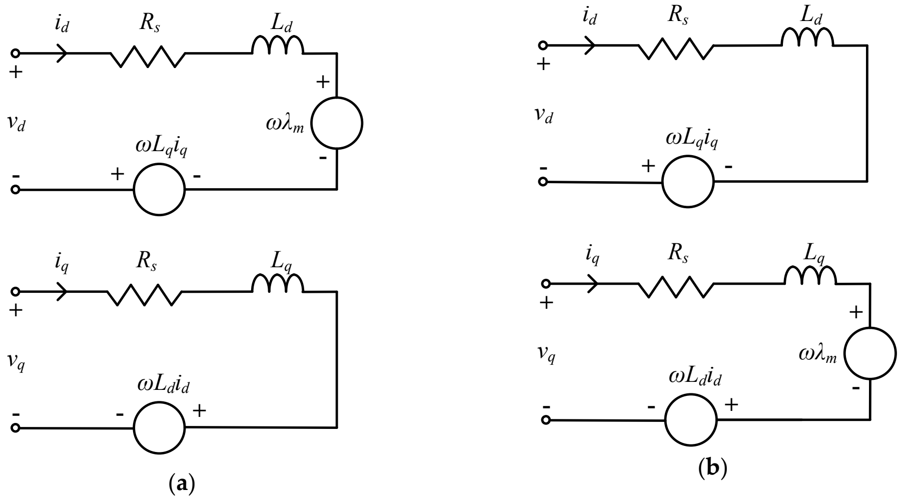

Figure 2. Equivalent circuits: (**a**) Type 1; (**b**) Type 2.

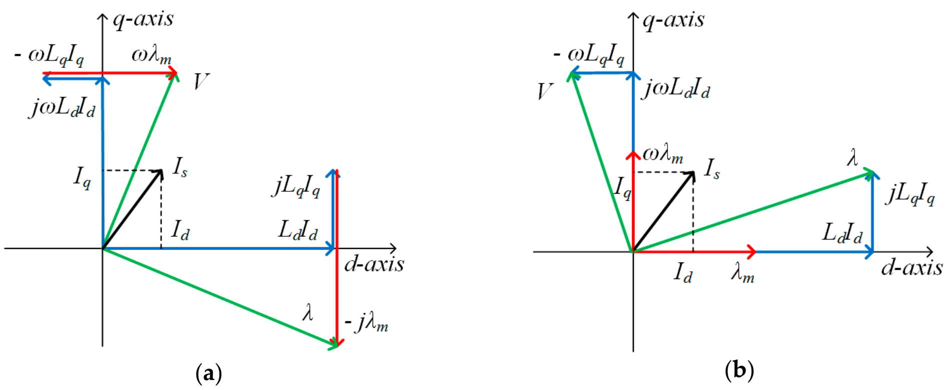

Figure 3. Phasor diagrams: (**a**) Type 1; (**b**) Type 2.

$$V = \omega\sqrt{(L_d I_d)^2 + \left(L_q I_q - \lambda_m\right)^2} \quad (5)$$

for Type 1 [30], and:

$$V = \omega\sqrt{(L_d I_d + \lambda_m)^2 + \left(L_q I_q\right)^2} \quad (6)$$

for Type 2.

Note that the "-" sign in front of λ_m in (3) and (5) indicates that the direction of this quantity is opposing $L_q I_q$, differing from the definition in [30].

The torque equations for Type 1 and Type 2 are respectively expressed as:

$$T = \frac{3N_m}{4}\left[\lambda_m I_d + (L_d - L_q) I_d I_q\right] \quad (7)$$

for Type 1 [29], and

$$T = \frac{3N_m}{4}\left[\lambda_m I_q + (L_d - L_q) I_d I_q\right] \quad (8)$$

for Type 2 [26].

Figure 4 illustrates the circle diagrams of these two types of motors. For the Type 1 motor with the first PM arrangement shown in Figures 1a, 3a and 4a indicate that the flux linkage generated by the q-axis current could cause the PM to be irreversibly demagnetized, especially for the thin PM. In contrast, for the Type 2 motor with the second PM arrangement shown in Figure 1b, the demagnetization on the PM can be avoided during maximum torque per ampere (MTPA) operation but may be possibly locally demagnetized during field weakening operation (this can be avoided by careful design), as shown in Figures 3b and 4b. This configuration may be subject to a lower power factor at low speed, but for medium and high-speed operations, the current phase advance would improve the power factor. On the other hand, inserting PM in the d-axis (flux paths) can decrease L_d and then decrease the reluctance torque so that the Type 2 motors would become closer to surface PM synchronous motors (SPMSMs). However, this requires a further investigation [31] and is not discussed here.

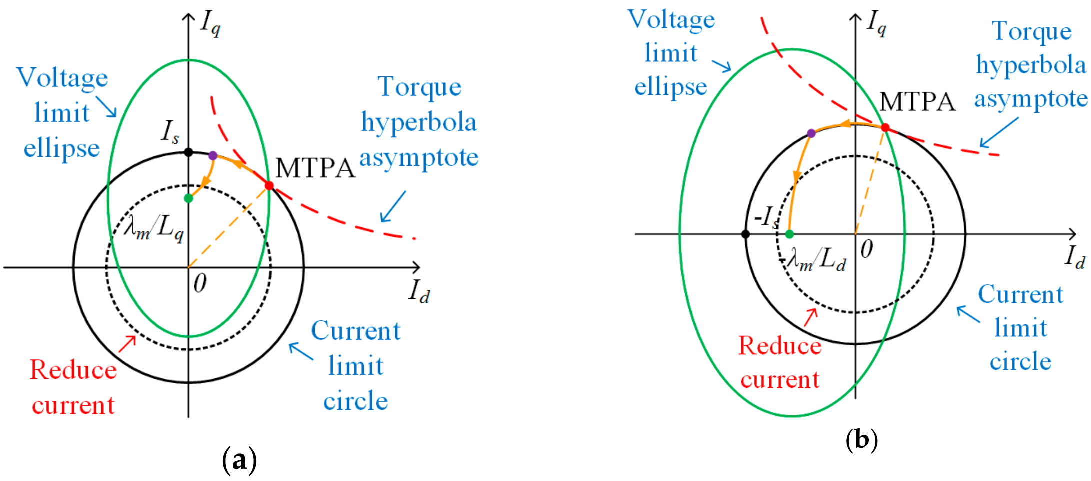

Figure 4. Circle diagrams: (**a**) Type 1; (**b**) Type 2.

The field weakening theory has been discussed in References [32,33] where ideally, the infinite speed could be achieved when the value of the armature current I_s is equal to the characteristic current I_{ch}. Practically, to increase the CPSR, I_s should be selected as close to I_{ch} as possible [32,34]. The motors in this paper have I_s greater than I_{ch} due to low the PM flux linkage by the limited PM quantity, as shown in Figure 4, where $I_{ch} = \lambda_m / L_q$ for Type 1 and $I_{ch} = \lambda_m / L_d$ for Type 2. There are two potential methods for improving the CPSR. The first method is to increase I_{ch} by using stronger or more magnet (higher λ_m) or changing the rotor configuration to reduce the q-axis or d-axis inductance for Type 1 or Type 2, respectively. However, this would lead to a redesign of the motors [35]. The second method is to reduce I_s (active reduction), as indicated in Figure 4, which however, should face a direct reduction of motor torque and power [24]. On the other hand, these motors can be operated in the maximum torque per voltage (MTPV) mode in which the current is reduced (passive reduction) when the speed increases. This would result in a partial overlap in the power-speed curves between the active and passive reductions of the excitation current in the field weakening region at high speed. This is explained in Section 4.3.

2.2. Configuration of Investigated Motors

As previously illustrated in Figure 1, for the rotor configuration of Type 1, the PMs are embedded along the flux barriers and located in the central part of each rotor pole. As indicated in Figure 1, P_{pm} is the magnet position from 1 to 4, W_{pm} is the magnet width and T_{pm} is the magnet thickness. For the Type 2 configuration, the PMs are arranged along the d-axis. Both types have the same PM positions viewed from the motor shaft (e.g., the PMs at Position 1 of Types 1 and 2 keep the same distance to the shaft). These arrangements of PM positions help to evaluate the effect of the PM directions (i.e., facing d- or q-axis). Note that, the magnetization of the PMs is all in the parallel pattern. The motor specifications and parameters are listed in Table 2, where the analysis at the peak current condition is for the purpose of exploring the capacity of the motors.

Table 2. Main specifications/parameters of models.

Parameter/ Specification	Unit	Value	Parameter/ Specification	Unit	Value
Desired peak power	kW	10	Stator diameter	mm	160
Number of phases	-	3	Rotor diameter	mm	94
Number of poles	-	4	Air-gap	mm	0.5
Number of slots	-	36	Stack length	mm	120
DC voltage	V	220	PM meterial	-	N35H
Maximum current	A	80	PM volume	mm^3	23040
Number of turns	turns	6	PM/Motor volume ratio	%	0.95

The performance of the prototype motor with Type 1 arrangement has been investigated with both the experiments and FEA simulations in Reference [23], where the results show that although the torque is high, this motor could not maintain the power and presented a low CPSR. This reduces its practical usefulness.

According to the previous discussion and the mathematical models described in the first part of this section, it is worthwhile to study the Type 2 motor as a potential alternative. Note that Section 2 mainly provides the mathematical background and briefly introduces the basic topologies of the two types of motor.

3. Comparative Analysis of Influence of PM Position

In this Section, the analyses on the effect of individual PM position on Type 1 and Type 2 motors using finite element analysis (FEA) were conducted. In these analyses, the no-load analysis aims to investigate the contribution of PM at different positions in the rotor to motor flux, and the on-load analysis is used to study the correlation between the PM position and armature excitation. No complete motor models are involved in this Section.

3.1. No-Load Operation Comparison

Base on the prototype motor in Reference [23], the PM pieces with a cross-sectional dimension of 1.5×8 mm were chosen and inserted into the PM positions from 1 to 4 (from inmost to outmost) in this study. Note that, all the PMs were fixed inside the flux barriers embracing them. In the beginning, to investigate the influence of the PM position, each time only one PM piece was placed at one of the above positions and the armature current was removed (no-load operation). The PM flux linkage and air-gap flux density B_g for each PM position of both types of motors are illustrated in Figure 5. As can be seen in Figure 5a,c, although the waveforms of the PM flux linkage for Type 1 seem to be different at different PM positions and the trend is unclear, the amplitudes are similar. On the other hand, the waveforms of B_g tend to spread out and the peak value deceases as the PM moves towards the inmost position. As shown in Figure 5b,d, all the PM flux linkage waveforms for Type 2 are basically trapezoidal and the amplitudes increase when the PM moves towards the outmost position. In addition, the waveforms of B_g are the same but the peak B_g increases when the PM moves towards the outmost position. The differences between the two types are significant. The PM position can be used on Type 1 to adjust the waveform of the PM flux linkage and both the waveform and amplitude of the air-gap flux density. For Type 2, this can adjust the amplitude of both the PM flux linkage and air-gap flux density.

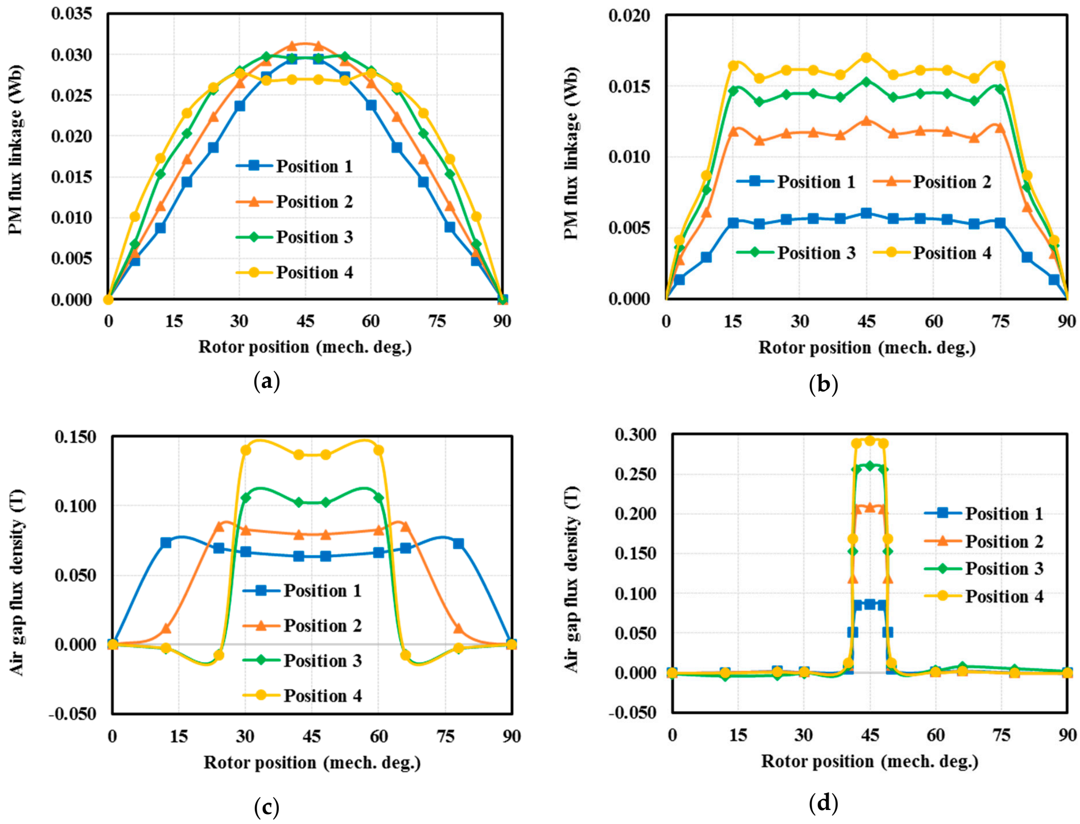

Figure 5. The PM flux linkage and air-gap flux density at no-load: (**a**) The PM flux linkage for Type 1; (**b**) the PM flux linkage for Type 2; (**c**) the air-gap flux density for Type 1; (**d**) the air-gap flux density for Type 2.

Table 3. Air-gap flux density for each PM position.

PM Position	1st	2nd	3rd	4th
Air-gap flux density for Type 1 (T)	0.056	0.060	0.067	0.075
Air-gap flux density for Type 2 (T)	0.025	0.059	0.074	0.083

The no-load peak flux density in the air gap for each PM position of both types is summarized in Table 3. For Type 1, the flux density at position 1 is the lowest (0.056 T) and that at position 4, is the highest (0.075 T). Similarly, for Type 2, the flux density at position 1 is the lowest (0.025 T) and that at position 4, is the highest (0.083 T). However, the lowest flux density for Type 2 is lower than Type 1, while the highest flux density for Type 2 is higher than Type 1. Thus, the no-load air-gap flux density for the Type 2 rotor seems to be more sensitive to positions. This is possibly because for Type 2, the PM flux is not blocked by the outer flux barriers while the blockage appears for Type 1. The revious analyses imply that for Type 1, the room for the PM flux can be more at the inward positions, i.e., larger or stronger PM [23], while for Type 2, more PM for the outward position could be used. In addition, the improvement of the PM flux linkage and air-gap flux density can be anticipated when the number of PM layers or the PM width increases, which is analyzed later.

3.2. On-Load Operation Comparison and Flux Balance Index

To fully investigate the influence of PM positions, the on-load operation is considered. Figure 6 shows the flux density distribution in the rotor with an 80 A peak current and maximum torque for each PM position (single PM each case). For Type 1, the most unbalanced flux density distribution occurs at the flux segments near the PMs (red circle) since the PM flux is obstructed by the surrounding flux barriers. The heavily unbalanced flux distribution may cause the PMs not to be utilized efficiently and lead to problems, such as local saturation, torque ripple or risk of demagnetization in motors [36]. For Type 2, the unbalance also occurs but appears to be lighter (dark blue circle) and the condition is almost the same for every PM position. This paper develops an index called the flux balance index to rate the degree of balance of flux distribution, which is given as:

$$K_u = \frac{B_u}{B_{rotor}} \cdot 100\% \tag{9}$$

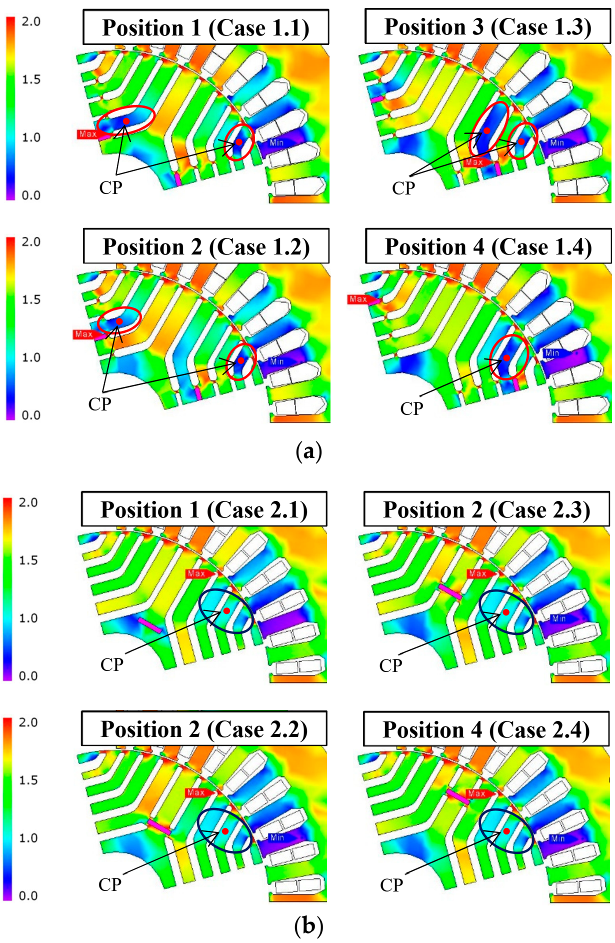

Figure 6. Comparison of the flux density distribution in rotors: (**a**) Type 1; (**b**) Type 2.

where B_u is the lowest flux density at the central point (CP) of the main unbalanced magnetic distribution zones as highlighted in Figure 6, and B_{rotor} is the average flux density in the rotor core obtained from a number of selected points (40 points in this paper) evenly spread out on the rotor core, as illustrated in Figure 7. The selection of these points only aims to represent the average flux density in the rotor without a particular criterion. Note that the determination of B_u and B_{rotor} does not take into account the singularities of the magnetic field, which do not represent the general magnetic distribution although these points are significant for saliency and the torque of motors [18,37]. The higher the flux balance index is, the better and more balanced magnetic distribution is in the rotor. The flux balance indices for various the PM positions of both types of motors are shown in Table 4. As can be seen, for Type 1, the flux balance index increases in the order of PM positions from 1 to 4 [Cases 1.1 to 1.4 in Figure 6a], indicating that the magnetic distribution would be better when the PM moves outward. In contrast, for Type 2, the unbalanced zones and the unbalanced condition do not seem to change as the PM position changes [Case 2.1 to 2.4 in Figure 6b]. This may be due to the fact that for such a configuration, the PM flux is not obstructed by the flux barriers. Furthermore, this unbalance is only caused by the armature reaction at load condition. As a result, Type 2 has a greater flux balance index than Type 1 does, meaning that the arrangement of PMs in Type 2 can be a decent choice to help improve the balance of the magnetic field.

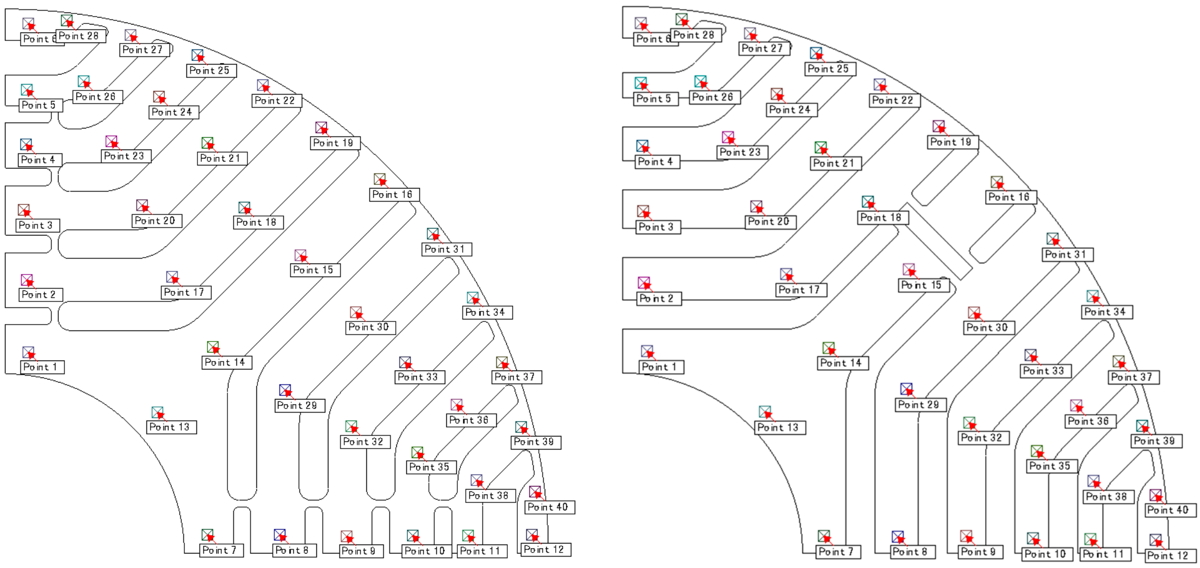

(a) (b)

Figure 7. The selected points for the rotor average flux density calculation: (**a**) Type 1; (**b**) Type 2, where the PM at position 4 is used as representative.

Table 4. The flux balance index of magnetic distribution in rotors.

PM Position	1st	2nd	3rd	4th
Lowest flux density for Type 1 (T)	0.262	0.302	0.355	0.372
Average flux density in rotor core for Type 1 (T)	1.104	1.111	1.103	1.120
Flux balance index, K_u for Type 1 (%)	23.74	27.19	32.18	33.23
Lowest flux density for Type 2 (T)	0.663	0.640	0.645	0.641
Average flux density in rotor core for Type 2 (T)	1.190	1.171	1.172	1.169
Flux balance index, K_u for Type 2 (%)	55.73	54.67	55.05	54.82

A brief comparison of the torque and torque ripple between the various PM positions of both types is shown in Figure 8. It can be seen that the torque ripple for Type 1 significantly changes with the PM positions, but this does not happen in Type 2. As previously mentioned, for Type 1, both the flux balance index and the locations of unbalance zones vary with the PM position, and the most unbalanced area occurs on the segment near the PM wherever it is placed (Figure 6a and Table 4). For Type 2, in contrast, both the flux balance index and the unbalanced zones seem to be independent of PM position (Figure 6b and Table 4). This indicates that the magnetic distribution in a Type 2 rotor is insensitive to the PM position, and this accounts for the invariant torque ripple with PM positions. In other words, for Type 1, the selection of PM position in a rotor should consider its effect on the magnetic distribution and thus torque ripple. For Type 2 motors, the torque ripple should not be a major concern for the placement of the PM. Note that, the torque output level is not affected significantly by the PM positions and motor types.

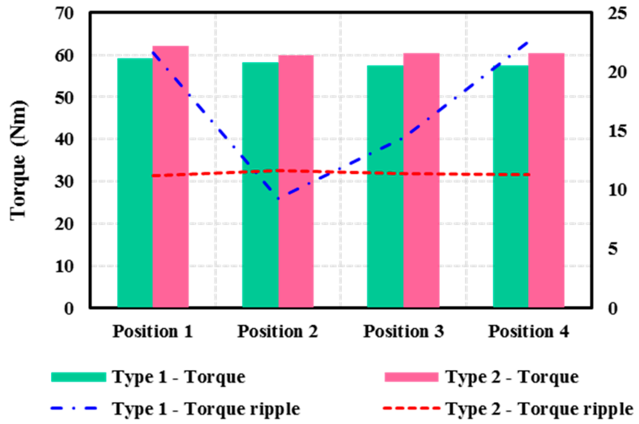

Figure 8. Torque production for each PM position.

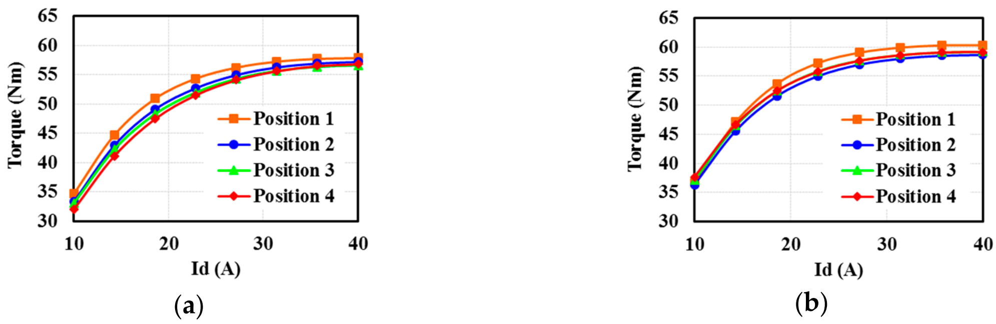

Figure 9. Torque production with Id for each PM position. (**a**) Type 1, (**b**) Type 2.

To fully compare the contribution of each PM position on torque production, the current is regulated in terms of the magnitude and phase advances with respect to the q-axis. The current I_q is kept at 70A and I_d is changed from 10 to 40 A, which considers the cross influence between the d- and q-axes and limits the armature within the peak value, i.e., 80 A. As the result shown in Figure 9, for Type 1, the torque decreases when the PM advances to position 4. In Type 2, although the highest air-gap flux density at position 4 is much higher than position 1, the torque is not much different at any positions. Besides, the highest torque can be generated by the PM at position 1 where the PM is separated from the flux barriers (no intersections), as shown in Figure 1b. However, the width of the PM is limited in this case. In Type 1, the most effective PM position in the torque production is the inward one [23] but it is limited by the possible room given in the rotor, and therefore the configuration with multiple PM layers is suitable for Type 1 to enhance the torque output. In Type 2, with the torque production at each PM position being similar and with the highest air-gap flux density occurring at position 4, this implies that the effective PM configuration is outwards, and the multiple PM layers construction may not be necessary.

In this section, small PM pieces have been used in both Type 1 and 2 motors for the comparison of the influence of PM position. Generally, the placement of these small PM pieces does not significantly change the rotor structure, especially for Type 1. However, the larger PM dimension (e.g., wider) or more pieces (e.g., multiple layers) would be more practical, and thus more variation in rotor configuration may require further assessment.

4. Comparative Analysis of Motor Characteristics

From the previous discussions, the comparison for various numbers of the PM layers as well as various the PM positions is presented. In this section, to fully investigate the performance and characteristics, six models broken down into the two types of motors discussed in Section 2 are created and shown in Figure 10, where Models 1, 2, and 3 are categorized in Type 1 and Models 4, 5, and 6 belong to Type 2. In these models, Models 1 and 4 have the PMs installed at position 1, Models 2 and 5 at position 4, and Models 3 and 6 at all the positions. As the previous analysis, the PMs are all magnetized in the parallel pattern. Note that these models can be treated as proper motors and the effect of various PM layouts (inmost, outmost and multiple layers) on motor inductances and torque production can be investigated through these rotor arrangements. All the models have the same main specifications and the PM thickness/volume. Their PM positions and dimensions are given in Table 5. Note that, the PM thickness is 1.5 mm, which is considered to be manufacturable [23,26].

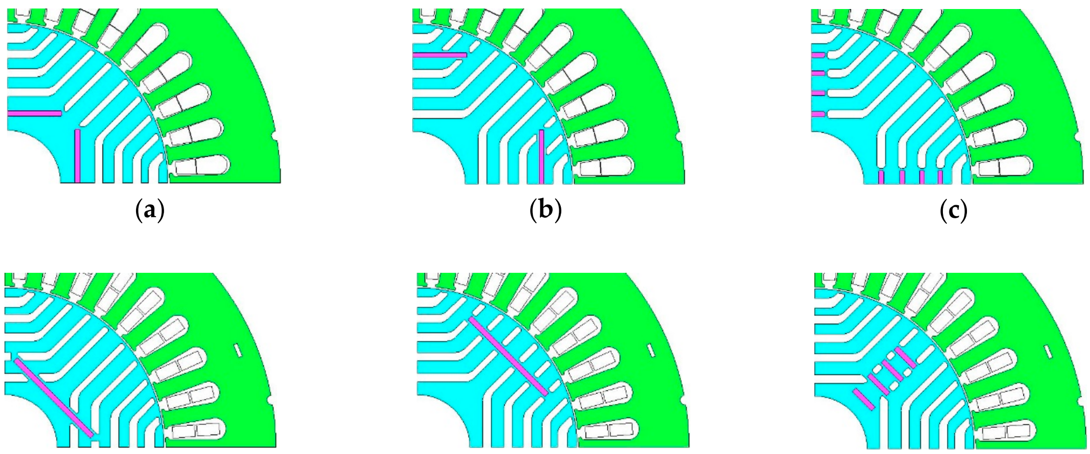

(**a**) (**b**) (**c**) (**d**) (**e**) (**f**)

Figure 10. Configurations of motor models: (**a**) Model 1; (**b**) Model 2; (**c**) Model 3; (**d**) Model 4; (**e**) Model 5; (**f**) Model 6.

Table 5. Position and dimension of PMs.

Items	Model 1	Model 2	Model 3	Model 4	Model 5	Model 6
PM position	1	4	1, 2, 3,4	1	4	1, 2, 3, 4
PM dimenssion	1.5 × 32 mm	1.5 × 32 mm	1.5 × 8 mm	1.5 × 32 mm	1.5 × 32 mm	1.5 × 8 mm

4.1. Motor Inductances

The inductance variation with the phase angle and magnitude of the current are shown in Figure 11, where the current angle was set to be zero for Figure 11c,d. Note that, these are the motor *d*- and *q*-axis inductances (L_{dm} and L_{qm}) with the presence of PMs rather than the ones without considering the PM flux, i.e., L_d and L_q (stator inductances) in Equations (3)–(8).

First, as shown in Figure 11a,c, for the Type 1 models (Models 1, 2 and 3), the inductance L_{dm} is the highest for Model 3 but not much higher than the others. The *q*-axis inductance L_{qm} is similar for Models 1, 2 and 3, which indicates that PM position does not significantly influence the electromagnetic characteristics of the motors. Conversely, as shown in Figure 11b,d, for the Type 2 models (Models

4, 5 and 6), the PM position has a great impact on L_{dm}, with the lowest for Model 5 because of the stronger flux created by the PM that limits the armature flux linkage. The inductance L_{qm} is similar for Models 4, 5 and 6. The above analysis shows that the PM position would be the most important design key for Type 2 motors.

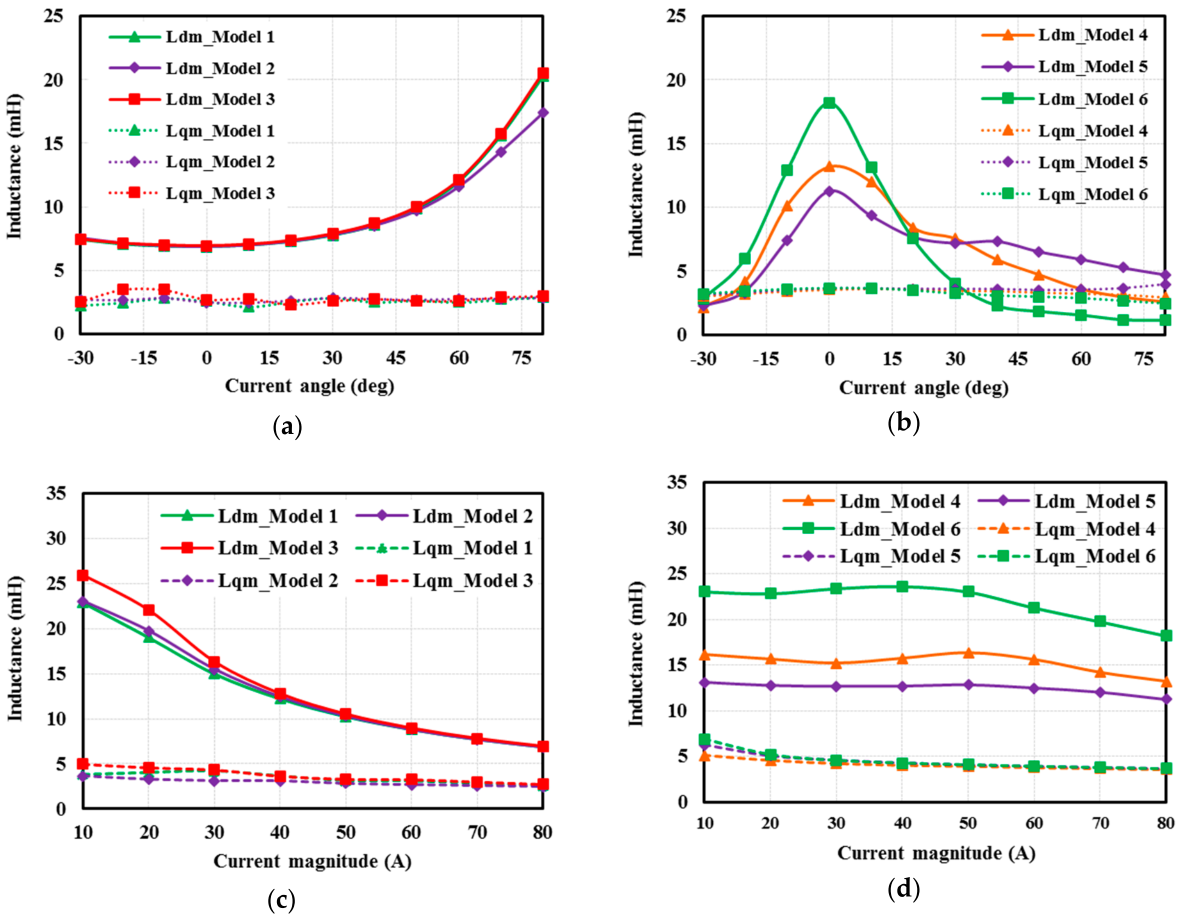

Figure 11. Inductance comparison: (**a**) Inductance versus current angle for Type 1; (**b**) Inductance versus current angle for Type 2; (**c**) Inductance versus current magnitude for Type 1; (**d**) Inductance versus current magnitude for Type 2.

Second, as the current magnitude increases, the inductance L_{dm} for the Type 1 models decreases rapidly while L_{qm} decreases gently, as shown in Figure 11c. However, as shown in Figure 11d, both L_{dm} and L_{qm} for Type 2 declines slightly with the current magnitude. This results in a small inductance difference ($L_{dm} - L_{qm}$) variation, especially for Model 5 whose L_{dm} and L_{qm} almost do not change. This may be attributed to the flux barriers that slightly brings down L_{qm}. Meanwhile, L_{dm} decreases mildly because of the alleviated *q*-axis magnetic saturation effects [38]. The insignificant inductance variation that may benefit sensorless control shows that fewer PM layers and placing the PM outwards would be more beneficial to the Type 2 motor design.

4.2. Torque Production

The torque production and torque components (i.e., PM/reluctance torques) are illustrated in Figure 12 and Table 6. To obtain the curves of torque versus the current angle using FEA, the initial rotor position can first be set up and based on that which the current is applied. Then, the current angle is regulated and swept through the prescribed range so that the output torque can be calculated for each current angle. As shown in Figure 12a, the torque production and torque components for all the models of Type 1 are almost similar. Of these cases, the multiple PM layers one, i.e., Model 3 is the best choice for the sake of its highest achieved total torque and PM torque ratio, as presented in Table 6. However, Model 1 should also be further considered since its torque is only slightly lower, taking the advantage of inmost PM arrangement, as discussed in the previous analysis. As shown in Figure 12b, the torque production and components are diverse for the models of Type 2, which agrees with the previous discussion. The case with the most outward PM and fewer PM layers, i.e. Model 5 would the best choice for its highest achieved total torque by making the most utilization of the PM compared to Models 4 and 6, as presented in Table 6. Furthermore, as presented in Table 6, the torque production of all the models of Type 1 is higher than every model of Type 2. This seems to indicate that the models of Type 1 have better torque production than Type 2. However, the high PM torque and its easy regulation by applying the various PM configurations (i.e., large PM torque difference between these investigated models) is a significant advantage of Type 2. On the other hand, for the Type 1 models, the torque is brought down to zero when the current angle is zero (i.e., I_d is zero) while for Type 2, the torque can only reduce to zero at the high current angle since the PM torque and the reluctance torque offset each other. Therefore, for the Type 2 motors, the armature excitation, i.e., the stator current I_s can be easily used to regulate the torque characteristics.

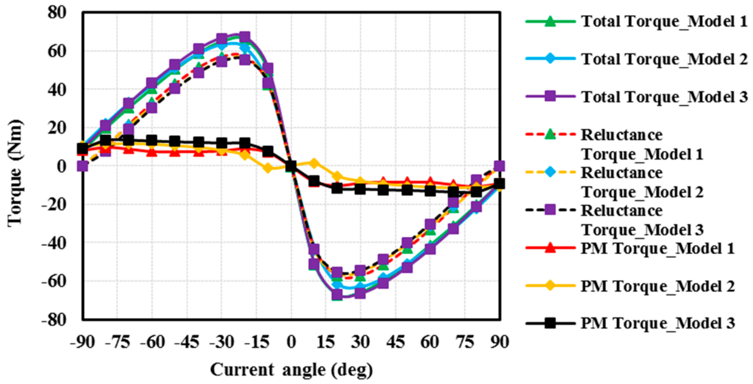

(**a**)

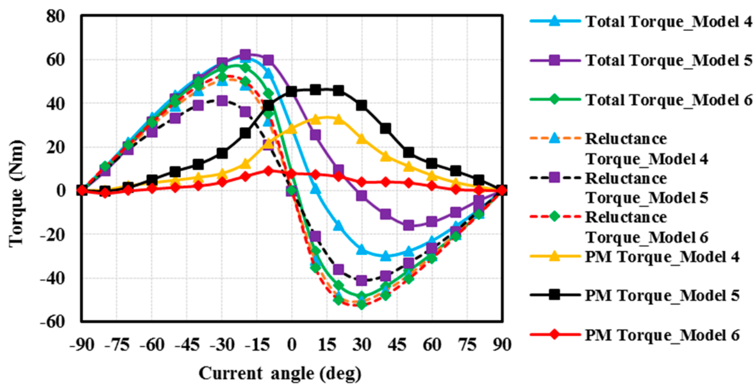

(**b**)

Figure 12. Torque production and components: (**a**) Type 1; (**b**) Type 2.

Table 6. Torque production and components.

Items	Model 1	Model 2	Model 3	Model 4	Model 5	Model 6
Maximum torque (Nm)	66.3	63.7	67.8	60.9	62.4	57.3
PM torque at maximum torque (Nm)	8.6	7.4	11.9	11.6	28.5	5.5
PM torque ratio (%)	13.0	11.6	17.6	19.0	45.7	9.6

4.3. Torque and Power-Speed Curves

As previously mentioned, the armature current I_s can be reduced to be close to I_{ch} to improve the speed range. The relationship between I_s and I_{ch} as I_s of Models 1, 3 and 5 varies and is presented in Table 7, where as expected, the I_s/I_{ch} ratio generally decreases as I_s decreases. Furthermore, Figures 13 and 14 show the comparison of torque-speed and power-speed curves between Models 1, 3 and 5, where a 220 V DC voltage is applied. In these curves, the rhombuses and circles denote the start- and end-points of the constant power region. The pink ones are for Model 3 and the blue ones are for Models 1 or 5. As can be seen in Figures 13 and 14, for the three models, the power-speed curves tend to converge at high speed and are partially overlapping. When I_s reduces to be close to I_{ch}, the CPSR of the motors improves but the torque and the power suffer some reduction. In Figure 13, the torque and power-speed curves of Model 1 are constantly slightly lower than Model 3 for the same I_s although the highest torque production is obtained when the PM is at the inmost position in the rotor. In contrast, although at a low speed operation, the torque production of Model 5 is lower than Model 3, but the difference decreases as I_s decreases. This results in an enhancement of the power-speed curves and CPSR for Model 5, which then surpasses Model 3, as seen in Figure 14. However, if I_s continues to reduce, e.g., I_s = 20 A, the CPSR of Model 5 cannot maintain the superiority to that of Model 3. This can be observed via the power-speed curves where there is an intersection point between these curves. The power corresponding to this point is denoted the intersection power, P_i. For such an intersection, if the required output power is greater than P_i, the CPSR of Model 5 is better than Model 3 and vice versa. Note that, as can be seen in Figure 14, this intersection point locates at the overlap of the MTPV control [33] regions of the target models so that this point no longer depends on the required current, but on the electromagnetic properties or the motor construction, i.e., PM flux linkage, inductance and I_{ch}.

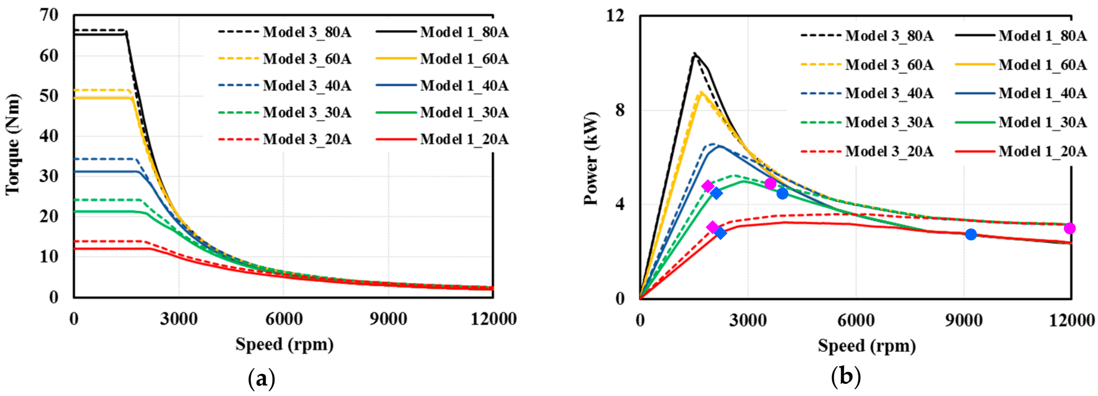

Figure 13. Field weakening comparison between Models 1 and 3: (**a**) Torque-speed curves; (**b**) Power-speed curves.

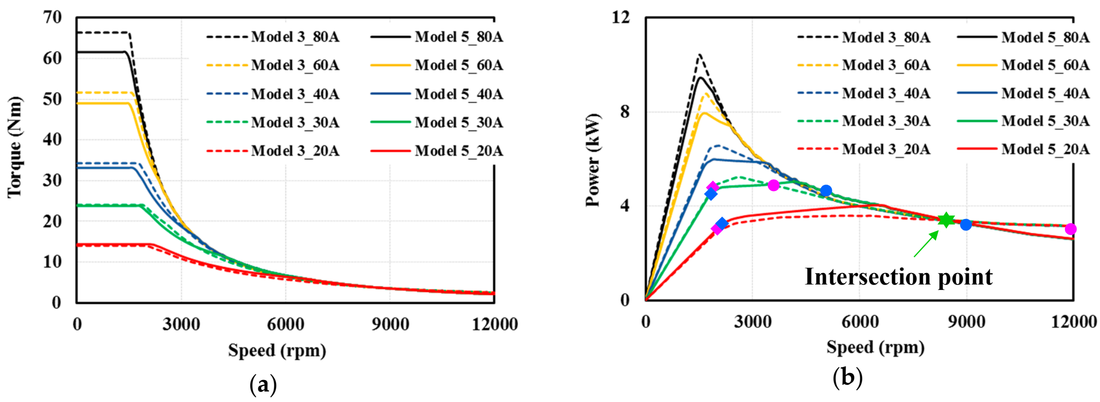

Figure 14. Field weakening comparison between Models 3 and 5: (**a**) Torque-speed curves; (**b**) Power-speed curves.

From the above discussions, with limited PM volume (less than common IPM motors), the selection of torque and power is closely related to desired motor speed range and needs to be chosen carefully by simultaneously considering the mechanical and electromagnetic characteristics of the motors and their applications. Although these motors are ideally infinite speed [16], the actual operating speed is limited. In addition, the selection of the PM positions and directions, e.g., moving PM from *q*-axis to *d*-axis in this paper, is the key to improve the performance of SynRMs with limited PM used.

Table 7. The constant power speed range (CPSR) analysis.

I_s (A)	80	60	40	30	20
I_{ch} (A) (Model 1)	18.9	17.1	13.7	10.2	9.4
I_s/I_{ch} (Model 1)	4.23	3.52	2.93	2.95	2.13
I_{ch} (A) (Model 3)	12.0	10.7	9.3	8.6	7.5
I_s/I_{ch} (Model 3)	6.67	5.59	4.28	3.50	2.68
I_{ch} (A) (Model 5)	19.7	17.2	15.1	14.2	13.7
I_s/I_{ch} (Model 5)	4.06	3.49	2.65	2.12	1.46

4.4. Demagnetization Analysis

The no-load PM flux linkage and air-gap flux density of Models 1, 3 and 5 are shown in Figure 15. It can be seen that when the PM width increases, the PM flux linkage and air-gap flux density of Type 2 (Model 5) increases significantly. This demonstrates the intensification of the magnetic field that is enabled by placing the PM along the *d*-axis instead of the *q*-axis. This can also explain the high PM torque ratio of Model 5 as presented in Table 6.

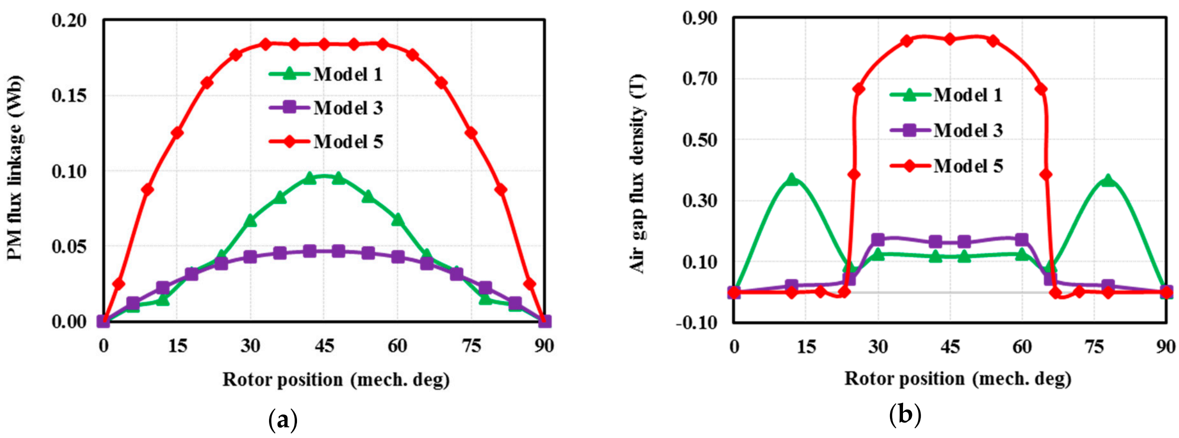

Figure 15. No-load magnetic characteristic. (**a**) PM flux linkage, (**b**) Air-gap flux density.

The distribution of flux density in the PMs of Models 1, 3 and 5 under the peak current at 120 °C are shown in Figure 16. The average flux density in the PMs at various temperatures are presented in Table 8. Note that, the demagnetization curves of N35H (PM material) are illustrated in Figure 17 [16,39]. It can be seen that the flux density in the PMs of Model 1 is very low, meaning that the PMs can be easily demagnetized. Moreover, the flux density in the PM of Model 1 is lower than Model 3 where the PMs are inserted at all positions. This implies that if only the inward PM position is used, an appropriate thickness of the PM should be carefully chosen to avoid irreversible demagnetization. The PMs in Models 3 and 5 have better demagnetization resistance compared to Model 1 since they possess better operating points, as the flux density presented in Table 8. Particularly, Model 5 possesses an advantage with an average PM flux density over 0.8 T. In contrast, the PMs in Model 3 can be locally demagnetized since their flux density are low, as shown in Figure 16. The key is the direction of the flux. In Type 1, the *q*-axis armature flux is opposing the PM flux and then reducing the flux at the *q*-axis. Instead, in Type 2, the *d*-axis armature flux and PM flux are in the same direction and then the d-axis flux is intensified. The motors that employ flux intensifying such as the Type 2 ones have been called the flux intensifying IPMSM [38,40,41]. However, in this paper, less PM is used for the rotor with a dominant reluctance torque, and therefore they should still be considered as a kind of SynRMs. They are named the FI-PMa-SynRM in this paper [26].

Overall, as investigated in this section, the layout with the PMs crossing the flux barriers have a decreased possibility to be demagnetized.

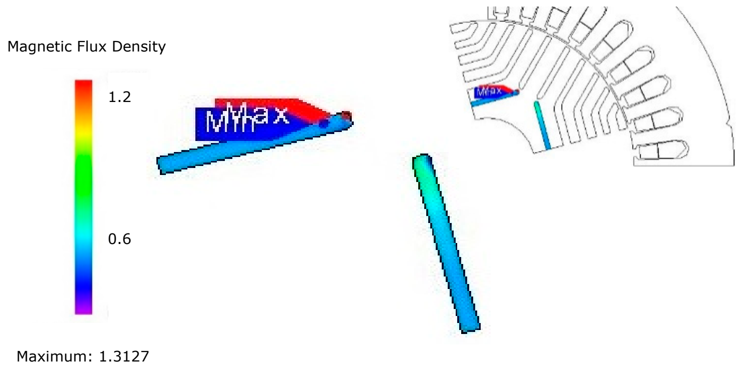

(**a**)

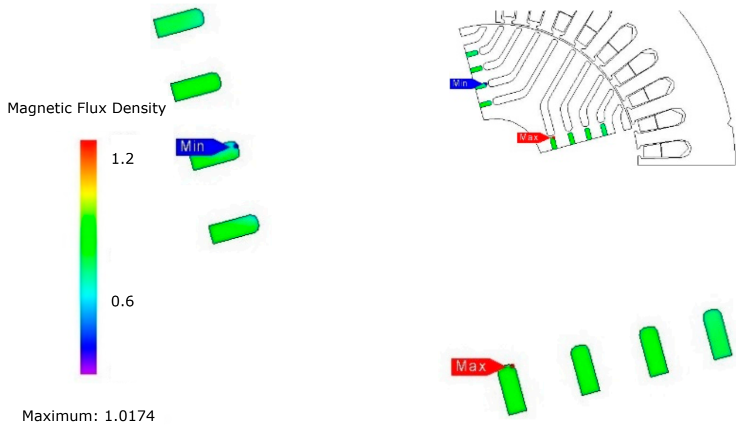

(**b**)

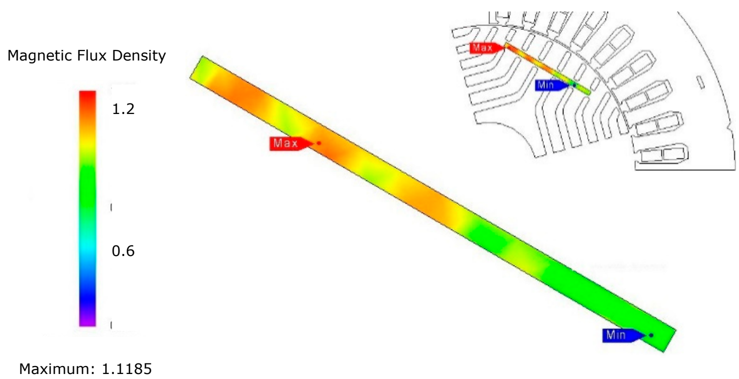

(**c**)

Figure 16. Flux density in PM at the 120 °C of temperature: (**a**) Model 1; (**b**) Model 3; (**c**) Model 5.

Table 8. Average flux density in PM.

Temperature	20 °C	90 °C	105 °C	120 °C	130 °C	155 °C
Model 1	0.403 T	0.354 T	0.342 T	0.327 T	0.273 T	0.133 T
Model 3	0.711 T	0.614 T	0.595 T	0.577 T	0.563 T	0.508 T
Model 5	0.912 T	0.869 T	0.860 T	0.852 T	0.845 T	0.828 T

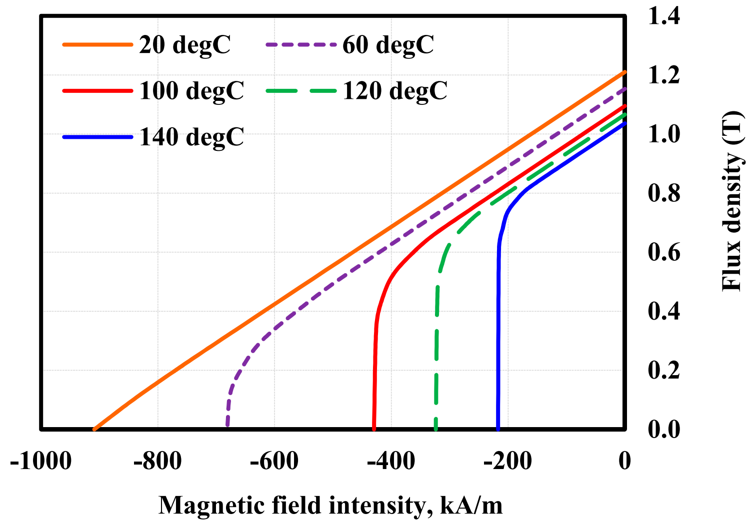

Figure 17. Demagnetization curves of N35H.

5. Discussion

Based on the previous analyses, some brief summaries are listed as follows.

- For the effect of the PM position, the outward PMs generally produce greater air-gap flux density but torque production does not exactly have the same trend.
- The PM position and its arrangement in the *d*- or *q*-axis have a great impact on flux distribution in the rotor where the *d*-axis PM arrangement possesses a higher flux balance index.
- The PM position has a greater impact on motor inductance of the Type 2 motor than the Type 1 one and the effect is approximately linear.
- Model 3 (conventional multiple-layer PMa-SynRM) has the highest torque production while Model 5 (FI-PMa-SynRM) has the most utilization of PM.
- Model 5 (FI-PMa-SynRM) is the best choice for demagnetization resistance while Model 1 is the worst one.
- For SynRM with a limited PM amount, the reduction of armature current I_s leads to an increase of CPSR but a trade-off with torque reduction should be considered.

The experimental studies were reported in [23], where the simulations were conducted using the same software package (JMAG). Since the focus of this paper is on the analysis and comparison of several types of SynRM rotors, therefore the experiments are not provided here.

6. Conclusions

In this paper, the analyses for six models of SynRMs with two different categories of PM layouts have been conducted, and their performance and electromagnetic characteristics have been comprehensively compared. From these analyses, it can be observed that the layout with PMs being arranged along the *q*-axis or embedded into the flux barriers has better torque production capability. For the other layout with the PM facing the *d*-axis or across the flux barriers, the advantages of SynRMs using a limited PM amount can be maintained and the inherent drawbacks, such as irreversible demagnetization, can be overcome. These indicate that, for SynRMs with a limited amount of PM added and placed along the *d*-axis would better make use of the PM. In addition, the PM arrangement at the inward position is a decent choice for SynRM with the *q*-axis PM, but the PM dimension should be calculated carefully to avoid irreversible demagnetization.

Author Contributions: D.-K.N. conceived and conducted the research and wrote the paper. M.-F.H. suggested the research topic, guided D.-K.N. to complete the research and helped edit and finalize the paper. M.-F.H. also provided the laboratory space and facilities for this study.

Funding: This work is supported by the Ministry of Science and Technology, Taiwan under project contracts MOST 108-2622-8-006-014 and 107-2622-E-006-005-CC2.

Acknowledgments: The authors would like to thank Thanh Anh Huynh for his help in this work. JSOL is also acknowledged for providing JMAG software.

Conflicts of Interest: The authors declare no conflicts of interest.

References

1. Lipo, T. Synchronous reluctance machines—A viable alternative for AC drives. *Electr. Mach. Power Syst.* **1991**, *19*, 659–671. [CrossRef]
2. Ozcelik, N.G.; Dogru, U.E.; Imeryuz, M.; Ergene, L.T. Synchronous reluctance motor vs. induction motor at low-power industrial applications: Design and comparison. *Energies* **2019**, *12*, 2190. [CrossRef]
3. Ibrahim, M.N.; Sergeant, P.; Rashad, E.M. Synchronous reluctance motor performance based on different electrical steel grades. *IEEE Trans. Magn.* **2015**, *51*, 1–4. [CrossRef]
4. Reddy, P.B.; El-Refaie, A.M.; Galioto, S.; Alexander, J.P. Design of synchronous reluctance motor utilizing dual-phase material for traction applications. *IEEE Trans. Ind. Appl.* **2017**, *53*, 1948–1957. [CrossRef]
5. Cai, S.; Jin, M.-J.; Hao, H.; Shen, J.-X. Comparative study on synchronous reluctance and PM machines. *COMPEL Int. J. Comput. Math. Electr. Electron. Eng.* **2016**, *35*, 607–623. [CrossRef]
6. Guan, Y.; Zhu, Z.Q.; Afinowi, I.A.A.; Mipo, J.C.; Farah, P. Design of synchronous reluctance and permanent magnet synchronous reluctance machines for electric vehicle application. *COMPEL Int. J. Comput. Math. Electr. Electron. Eng.* **2016**, *35*, 586–606. [CrossRef]
7. Carraro, E.; Degano, M.; Morandi, M.; Bianchi, N. PM synchronous machine comparison for light electric vehicles. In Proceedings of the IEEE International Electric Vehicle Conference (IEVC), Florence, Italy, 17–19 December 2014; pp. 1–8.
8. Ibrahim, M.N.F.; Rashad, E.; Sergeant, P. Performance comparison of conventional synchronous reluctance machines and PM-assisted types with combined star-delta winding. *Energies* **2017**, *10*, 1500. [CrossRef]
9. Bianchi, N.; Fornasiero, E.; Soong, W. Selection of PM flux linkage for maximum low-speed torque rating in a PM-assisted synchronous reluctance machine. *IEEE Trans. Ind. Appl.* **2015**, *51*, 3600–3608. [CrossRef]
10. Guglielmi, P.; Boazzo, B.; Armando, E.; Pellegrino, G.; Vagati, A. Permanent magnet minimization in PM-assisted synchronous reluctance motors for wide speed range. *IEEE Trans. Ind. Appl.* **2013**, *49*, 31–41. [CrossRef]
11. Bianchi, N.; Mahmoud, H.; Bolognani, S. Fast synthesis of permanent magnet assisted synchronous reluctance motors. *IET Electr. Power App.* **2016**, *10*, 312–318. [CrossRef]
12. Niazi, P.; Toliyat, H.A.; Cheong, D.-H.; Kim, J.-C. A low-cost and efficient permanent-magnet-assisted synchronous reluctance motor drive. *IEEE Trans. Ind. Appl.* **2007**, *43*, 542–550. [CrossRef]
13. Lee, J.H.; Jang, Y.J.; Hong, J.P. Characteristic analysis of permanent magnet-assisted synchronous reluctance motor for high power application. *J. Appl. Phys.* **2005**, *97*, 10Q503. [CrossRef]
14. Huynh, T.A.; Hsieh, M.F. Performance analysis of permanent magnet motors for electric vehicles (EV) traction considering driving cycles. *Energies* **2018**, *11*, 1385. [CrossRef]
15. Cai, H.; Guan, B.; Xu, L. Low-Cost ferrite PM-Assisted synchronous reluctance machine for electric vehicles. *IEEE Trans. Ind. Electron.* **2014**, *61*, 5741–5748. [CrossRef]
16. Huynh, T.A.; Hsieh, M.-F. Comparative study of PM-assisted SynRM and IPMSM on constant power speed range for EV applications. *IEEE Trans. Magn.* **2017**, *53*, 1–6. [CrossRef]
17. Vagati, A. Synchronous Reluctance Electrical Motor Having a Low Torque-Ripple Design. U.S. Patent 5,818,140, 6 October 1998.

18. Ferrari, M.; Bianchi, N.; Fornasiero, E. Rotor saturation impact in synchronous reluctance and PM assisted reluctance motors. In Proceedings of the IEEE Energy Conversion Congress and Exposition (ECCE), Denver, CO, USA, 15–19 September 2014; pp. 1235–1242.
19. Binns, K.J.; Lawrenson, P.J.; Trowbridge, C.W. *The Analytical and Numerical Solution of Electric and Magnetic Fields*; Wiley: Chichester, UK, 1992.
20. Moghaddam, R.R. Synchronous Reluctance Machine (SYNRM) in Variable Speed Drives (VSD) Applications. Ph.D. Thesis, KTH Royal Institute of Technology, Stockholm, Sweden, 2011.
21. Morimoto, S.; Sanada, M.; Takeda, Y. Performance of PM-Assisted synchronous reluctance motor for high-efficiency and wide constant-power operation. *IEEE Trans. Ind. Appl.* **2001**, *37*, 1234–1240. [CrossRef]
22. Imamura, K.; Sanada, M.; Morimoto, S.; Inoue, Y. Improvement of characteristics by flux barrier shape and magnet thickness of IPMSM with Dy-free rare-earth magnet. In Proceedings of the 15th European Conference on Power Electronics and Applications (EPE), Lille, France, 2–6 September 2013; pp. 1–10.
23. Huynh, T.A.; Hsieh, M.-F.; Shih, K.-J.; Kuo, H.-F. An investigation into the effect of PM arrangements on PMa-SynRM performance. *IEEE Trans. Ind. Appl.* **2018**, *54*, 5856–5868. [CrossRef]
24. Pellegrino, G.; Vagati, A.; Guglielmi, P. Design tradeoffs between constant power speed range, uncontrolled generator operation, and rated current of IPM motor drives. *IEEE Trans. Ind. Appl.* **2011**, *47*, 1995–2003. [CrossRef]
25. Prins, M.H.A.; Kamper, M.J. Design optimisation of field-intensified permanent magnet machine. In Proceedings of the IEEE International Conference on Electrical Machines (ICEM), Berlin, Germany, 2–5 September 2014; pp. 117–123.
26. Ngo, D.-K.; Hsieh, M.-F.; Huynh, T.A. Torque enhancement for a novel flux intensifying PMa-SynRM using surface-inset permanent magnet. *IEEE Trans. Magn.* **2019**, *55*, 8106108. [CrossRef]
27. Pillay, P.; Krishnan, R. Modeling of permanent magnet motor drives. *IEEE Trans. Ind. Electron.* **1988**, *35*, 537–541. [CrossRef]
28. Morimoto, S.; Takeda, Y.; Hatanaka, K.; Tong, Y.; Hirasa, T. Designand control system of inverter-driven permanent magnet synchronous motors for high torque operation. *IEEE Trans. Indus. Appl.* **1993**, *29*, 1150–1155. [CrossRef]
29. Baek, J.; Bonthu, S.S.R.; Choi, S. Design of five-phase permanent magnet assisted synchronous reluctance motor for low output torque ripple applications. *IET Electr. Power App.* **2016**, *10*, 339–346. [CrossRef]
30. Lee, J.H.; Kim, J.C.; Hyun, D.S. Effect analysis of magnet on Ld and Lq inductance of permanent magnet assisted synchronous reluctance motor using finite element method. *IEEE Trans. Magn.* **1999**, *35*, 1199–1202. [CrossRef]
31. Ngo, D.-K.; Hsieh, M.-F. Analysis of flux intensifying effect on synchronous motors applied to electric scooter. In Proceedings of the IEEE Vehicle Power and Propulsion Conference (IEEE-VPPC), Hanoi, Vietnam, 14–17 October 2019.
32. Jahns, T.M. Flux-weakening regime operation of an interior permanent-magnet synchronous motor drive. *IEEE Trans. Ind. Appl.* **1987**, *23*, 681–689. [CrossRef]
33. Soong, W.L.; Miller, T.H.E. Field-weakening performance of brushless synchronous AC motor drives. *IEE Proc. Electr. Power Appl.* **1994**, *141*, 331–340. [CrossRef]
34. Jahns, T.M.; Kliman, G.B.; Neumann, T.W. Interior permanent-magnet synchronous motors for adjustable-speed drives. *IEEE Trans. Ind. Appl.* **1986**, *22*, 738–747. [CrossRef]
35. Barcaro, M.; Bianchi, N.; Magnussen, F. Permanent-magnet optimization in permanent-magnet-assisted synchronous reluctance motor for a wide constant-power speed range. *IEEE Trans. Ind. Electron.* **2012**, *59*, 2495–2502. [CrossRef]
36. Kim, W.-H.; Kim, K.-S.; Kim, S.-J.; Kang, D.-W.; Go, S.-C.; Chun, Y.-D.; Lee, J. Optimal PM design of PMA-SynRM for wide constant-power operation and torque ripple reduction. *IEEE Trans. Magn.* **2009**, *45*, 4660–4663. [CrossRef]
37. Ferrari, M.; Bianchi, N.; Doria, A.; Fornasiero, E. Design of synchronous reluctance motor for hybrid electric vehicles. *IEEE Trans. Ind. Appl.* **2015**, *51*, 3030–3040. [CrossRef]
38. Zhu, X.; Yang, S.; Du, Y.; Xiang, Z.; Xu, L. Electromagnetic performance analysis and verification of a new flux-intensifying permanent magnet brushless motor with two-layer segmented permanent magnets. *IEEE Trans. Magn.* **2016**, *52*, 1–4. [CrossRef]

39. N35H—Arnold Magnetic Technologies. Available online: https://www.arnoldmagnetics.com/wp-content/uploads/2017/11/N35H-151021.pdf (accessed on 23 July 2019).
40. Zhu, X.; Wu, W.; Yang, S.; Xiang, Z.; Quan, L. Comparative design and analysis of new type of flux-intensifying interior permanent magnet motors with different q-axis rotor flux barriers. *IEEE Trans. Energy Convers.* **2018**, *33*, 2260–2269. [CrossRef]
41. Limsuwan, N.; Shibukawa, Y.; Reigosa, D.D.; Lorenz, R.D. Novel design of flux-intensifying interior permanent magnet synchronous machine suitable for self-sensing control at very low speed and power conversion. *IEEE Trans. Ind. Appl.* **2011**, *47*, 2004–2012. [CrossRef]